

Geometric Calibration for X-ray Fluorescence Tomography using Multi-Support Consistency

Meo van Duijnen Montijn, Jérôme Lesaint, Jean Michel Létang, and Simon Rit

Abstract—We propose a novel geometric calibration approach for computed tomography (CT) based on data consistency conditions that rely solely on sinogram supports, i.e., the regions where the sinogram values are non-zero. This approach enables the estimation of shifts, from which the center of rotation may also be directly inferred. The approach is agnostic to attenuation and applies to sets of supports arising from different spatial, spectral, and other measurement domains. While the formulation is general, X-ray fluorescence CT serves as the primary application considered in this work. Numerical simulations demonstrate the accuracy of the proposed approach.

I. INTRODUCTION

GEOMETRIC calibration is a prerequisite for accurate reconstructions in all computed tomography (CT) modalities. Errors in the acquisition geometry—such as misestimated centers of rotation or uncorrected sample motion—cause reconstruction artifacts and loss of resolution. In transmission-based tomography, analytical calibration approaches grounded in data consistency conditions (DCCs), most notably those derived from the Helgason-Ludwig conditions [1], provide data-driven means to address these issues. Such methods enable center-of-rotation determination and shift correction directly from projection data [2], eliminating the need for external markers or heuristic alignment procedures.

However, Helgason-Ludwig DCCs rely on assumptions that may be violated in modalities governed by multiple interaction mechanisms, most notably X-ray fluorescence CT (XFCT). In X-ray fluorescence, atoms are excited through X-ray irradiation and subsequently emit secondary fluorescence photons isotropically. In XFCT, fluorescence photons emitted following X-ray excitation are recorded as functions of translation and rotation and, after spectral fitting, yield elemental sinograms from a single measurement, as illustrated in Fig. 1. A major difficulty, however, is that both the incident beam and the emitted fluorescence are attenuated along their respective paths, thereby eliminating the general validity of existing analytical calibration approaches.

Crucially, although attenuation alters sinogram intensities, it may not affect the sinogram support, so calibration-relevant

M. van Duijnen Montijn is with ESRF, The European Synchrotron, 71 Avenue des Martyrs, CS 40220, 38043 Grenoble Cedex 9, France, and with INSA Lyon, Université Claude Bernard Lyon 1, CNRS, Inserm, CREATIS UMR 5220, U1294, F-69621 Villeurbanne, France (e-mail: meo.van-duijnen-montijn@esrf.fr).

J. Lesaint is with ESRF, The European Synchrotron, 71 Avenue des Martyrs, CS 40220, 38043 Grenoble Cedex 9, France (e-mail: jerome.lesaint@esrf.fr).

J. M. Létang and S. Rit are with INSA Lyon, Université Claude Bernard Lyon 1, CNRS, Inserm, CREATIS UMR 5220, U1294, F-69621 Villeurbanne, France (e-mail: jean.letang@insa-lyon.fr; simon.rit@creatis.insa-lyon.fr).

Manuscript received January 28, 2026.

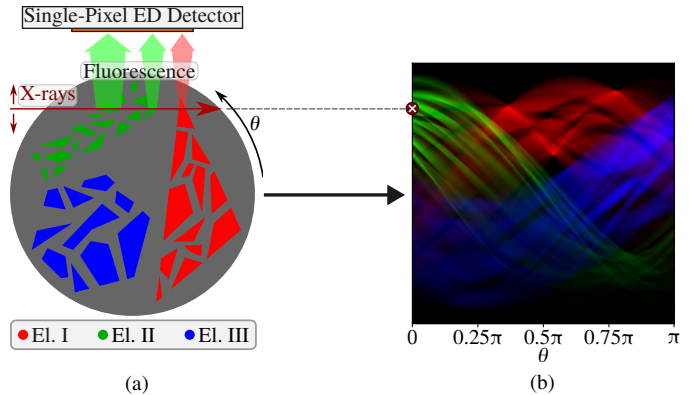


Fig. 1. XFCT: (a) Experimental setup in which an X-ray pencil beam traverses the sample at each projection angle and excites atoms in a phantom comprising distinct elements (here, three), generating fluorescence photons that are recorded by a single-pixel energy-dispersive (ED) detector positioned normal to the beam direction. (b) Combined X-ray fluorescence sinograms exhibiting attenuation effects. The white cross indicates the pencil beam position in (a).

information may be preserved even in the presence of unknown attenuation. Early work showed that single-sinogram support boundaries could be used for coarse geometric calibration [3]. More recently, accurate calibration has been achieved by heuristically matching large sets of supports via iterative reprojection [4], but at high computational cost, as repeated image reconstructions are required, and without an analytical foundation. Here, we extend upon the DCCs introduced in [3] to obtain an analytical, attenuation-agnostic calibration approach using sets of supports. The proposed approach enables direct estimation of geometric shifts and the center of rotation. Although the formulation is general, XFCT is used as the primary validation modality.

II. MATHEMATICS

In XFCT, one collects sinograms for different elements and possibly at different out-of-plane offsets. From each sinogram, a sinogram support $Y \subset \mathbb{R}^2$, defined by its nonzero entries, can be extracted, together forming the set \mathbb{Y} . Each sinogram support Y in this set is determined by the projection of a convex envelope $X \subset \mathbb{R}^2$ in object space, with the corresponding set of envelopes denoted by \mathbb{X} , and is related through the mapping $\mathcal{R}_{\text{sup}} : X \mapsto Y$ as illustrated in Fig. 2. For each element of \mathbb{Y} , the outer sinogram boundaries $h_Y^+(\theta)$ and $h_Y^-(\theta)$ may be extracted, denoting the lower and upper borders, respectively, in the direction of translation. Although

additional boundaries may in principle be identified, they are not considered in this work.

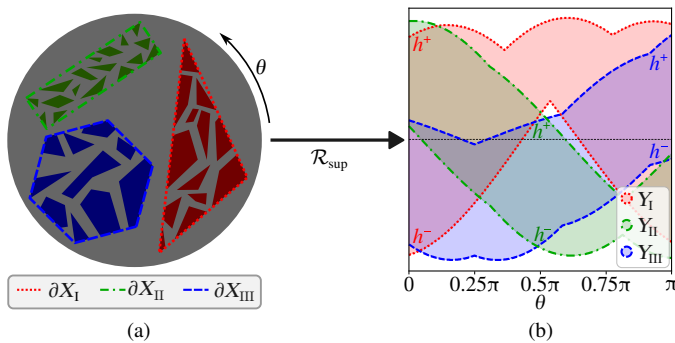


Fig. 2. Convex envelopes (X), support sinograms (Y) and their mapping: (a) Three spatial domains containing different fluorescing elements, with the borders of their convex envelopes (∂X) highlighted. (b) The corresponding fluorescence support sinograms and their upper and lower boundaries are denoted h^+ and h^- , respectively.

The main sinogram boundaries are traced, for each projection angle, by the extreme points of the object's convex envelope in the translational dimension. The boundaries of the convex envelope in object space are therefore directly related to the boundaries of its support sinogram. Since the object-space boundaries correspond to those of a convex shape, their radii of curvature do not change sign between different boundary points on the same side of the sinogram. It was shown in [3] that these radii of curvature are related to the boundaries of the support sinograms via

$$\rho_X^\pm(\theta) = \mathcal{L}h_Y^\pm(\theta), \quad \pm\rho_X^\pm(\theta) \geq 0, \quad (1)$$

where the linear operator is defined as

$$\mathcal{L} := \text{Id} + \frac{\partial^2}{\partial\theta^2}, \quad (2)$$

and Id is the identity operator. The functions $\rho_X^+(\theta)$ and $\rho_X^-(\theta)$ correspond to the + and - branches of Eq. 1 and denote the radii of curvature at the upper and lower extreme points, respectively, of the convex envelope X at angle θ . Boundaries that are not twice differentiable are interpreted in the sense of distributions. Two examples illustrating the validity of Eq. 1 are shown in Fig 3.

A. Perturbations

In-plane perturbations manifest themselves as angle-dependent shifts $\Delta(\theta)$ in the translational dimension, yielding perturbed sinogram boundaries

$$\tilde{h}_Y^\pm(\theta) := h_Y^\pm(\theta) + \Delta(\theta). \quad (3)$$

Such perturbations may violate the DCCs of Eq. 1. However, enforcing these conditions by applying shifts to a perturbed sinogram does not, in general, lead to a unique solution. For each sinogram Y , there may exist an entire set of admissible shifts \mathbb{A}_Y that restore the DCCs when applied. Since the true shifts are identical for all Y and are contained in each of these sets, it follows that

$$\Delta(\theta) \in \mathbb{A} := \bigcap_{Y \in \mathbb{Y}} \mathbb{A}_Y, \quad (4)$$

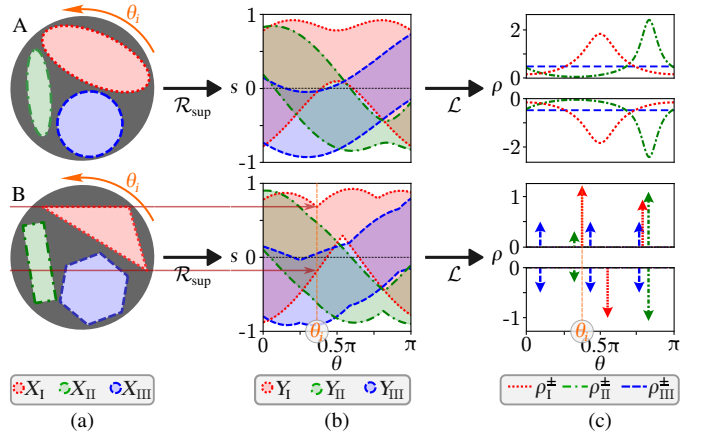


Fig. 3. Radii of curvature for two phantoms with a highlighted case. (a) Phantoms A and B, exhibiting jagged and smooth convex envelopes X of fluorescent supports, respectively, within a gray capillary. The two pencil beams correspond to irradiated extreme points of X_I for phantom B at angle θ_i with infinity (top) and zero (bottom) radii of curvature. (b) Support sinograms. The vertical dashed line highlights Y_I of phantom B at angle θ_i , featuring a cusp and a sinusoidal segment at the boundaries. (c) Corresponding radii of curvature (ρ^+ and ρ^- in top and bottom plots, respectively), with arrows indicating Dirac delta contributions.

where \mathbb{A} denotes the ambiguity in $\Delta(\theta)$ when considering the full set \mathbb{Y} of sinogram supports Y .

B. Ambiguity analysis

Combining Eqs. 1 and 3 yields the relation

$$\pm\rho_X^\pm(\theta) = \pm\mathcal{L}\left[\tilde{h}_Y^\pm(\theta) - \Delta(\theta)\right] \geq 0. \quad (5)$$

Taking both signs of this equation into account then leads to

$$\mathcal{L}\tilde{h}_Y^-(\theta) \leq \mathcal{L}\Delta(\theta) \leq \mathcal{L}\tilde{h}_Y^+(\theta) \quad \forall Y \in \mathbb{Y}. \quad (6)$$

The sets of admissible shifts \mathbb{A}_Y thus comprises all functions $\Delta(\theta)$ that satisfy this condition. The properties of this set have been investigated: any two entries differ only in their odd-frequency Fourier components, whose amplitudes are constrained and mutually linked. Evaluating this set, for example, for the case in which X is a circle, yields the ambiguity in the object domain corresponding to the family of Reuleaux polygons [5], which themselves, consistently, exist only for odd orders. These and related properties are exploitable, but are left for future work. Since \mathbb{A}_Y may differ for each Y , an increasing number of sinograms in the set \mathbb{Y} may progressively constrain the ambiguity in $\Delta(\theta)$ via Eq. 4, although not every additional element necessarily leads to a further reduction. Neglecting a fundamental harmonic component in the shifts, which merely induces a global displacement of the reconstruction, a criterion can be derived under which the intersection of admissible shifts reduces to a singleton. For this to occur, the set \mathbb{Y} must contain objects X with extreme points having zero-radius of curvature for a sufficient amount of projection angles. E.g., this is satisfied by phantom B alone (Fig 3). If \mathbb{Y} fails to satisfy this criterion for uniqueness—which will likely be difficult to assess in practice—an ambiguity in the shifts remains. Nevertheless, this ambiguity may still be sufficiently constrained for practical purposes and may furthermore be determined using only the perturbed projection data.

III. METHODS

XFCT acquisitions were simulated on two phantoms, as illustrated in Fig. 3a, using 256 translational steps and 360 rotational steps over a half-turn. Each phantom contained three convex envelopes emitting different fluorescence, within an attenuating capillary. The exact separation, whether in the spatial or energy domain, is irrelevant, provided that the supports are distinguishable, however. The simulations were carried out using the PyCorrectedEmissionCT package (<https://pypi.org/project/correct/>) [6]. Fluorescence sinograms were generated by assigning three arbitrarily chosen fluorescence-emitting elements (I, II, III) to the supports, and by attaching attenuation maps to both the supports and the capillary. Shifts were modeled as semi-random combinations of trigonometric functions superimposed on noise. The sinograms were then perturbed by applying these shifts via linear interpolation of the pixel intensities, as shown in Fig. 4. Determining a solution

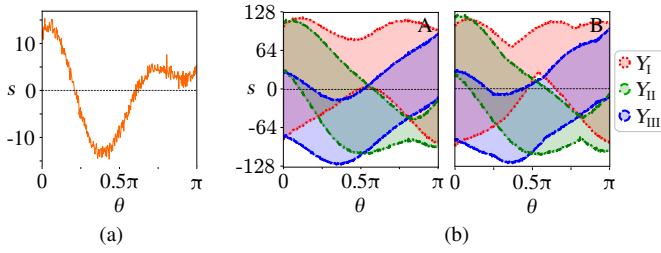


Fig. 4. (a) Simulated perturbation and (b) corresponding perturbed support sinograms for phantoms A and B.

for the shifts under the constraint of Eq. 6 requires evaluating second-order derivatives of the perturbed boundary positions. Direct computation of these derivatives using finite differences, however, is numerically unstable. In the sinogram domain, each point in object space traces a fundamental (co)sine of period 2π . For every boundary point, there must therefore exist a cosine that passes through it and remains entirely within the sinogram support. This condition corresponds to the edge case of Eq. 1, for which $\mathcal{L}h_Y^\pm(\theta) = 0$. Each such cosine has only a single degree of freedom, as it is constrained to pass through a given boundary point. Accordingly, for the perturbed boundary points of a sinogram Y at projection index i , after applying a candidate shift $(\hat{\Delta}_i)$, this function can be expressed as a cosine with relative phase ϕ via

$$m_{Y,i}^\pm(\hat{\Delta}_i, \phi_{Y,i}^\pm, \theta) := \frac{\tilde{h}_{Y,i}^\pm - \hat{\Delta}_i}{\cos \phi_{Y,i}} \times \cos(\theta - \theta_i + \phi_{Y,i}^\pm), \quad (7)$$

where the amplitude (in front of the cosine) is chosen such that the function passes through the boundary point, as illustrated in Fig. 5a. The objective is to minimize violations where these functions leave the sinogram support. Denoting the discrete arrays of the perturbed boundaries, shifts, and projection angles by \tilde{h}_Y^\pm , $\hat{\Delta}$ and θ , respectively, these violations are quantified by the violation vectors

$$\begin{aligned} v_{Y,i}^\pm(\hat{\Delta}, \phi_{Y,i}^\pm) &:= \\ &\max \left(m_{Y,i}^\pm(\hat{\Delta}_i, \phi_{Y,i}^\pm, \theta) - (\tilde{h}_Y^\pm - \hat{\Delta}), \mathbf{0} \right) \quad (8) \\ &+ \min \left(m_{Y,i}^\pm(\hat{\Delta}_i, \phi_{Y,i}^\pm, \theta) - (\tilde{h}_Y^\pm - \hat{\Delta}), \mathbf{0} \right), \end{aligned}$$

where the first and second terms track the function passing out of the upper and lower support boundaries, respectively. This then gives the entries and magnitudes of such violations,

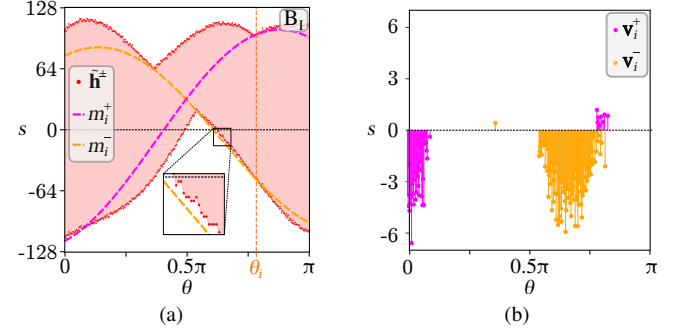


Fig. 5. Cosine fitting at angle θ_i for element I of phantom B: (a) Perturbed support sinogram with the best-fitting cosines (m_i^\pm). (b) Violations of the fitted cosines (v_i^\pm), i.e. cosine exceedances as defined in Eq. 8, with zero-valued entries omitted.

as illustrated in Fig. 5b. These vectors must be minimized simultaneously over all projections and for all entries of \mathbb{Y} . To achieve this, we define a cost function depending on the candidate shift $\hat{\Delta}$ and on the complete set of relative phases $\Phi := \{\phi_Y^+, \phi_Y^-\}_{Y \in \mathbb{Y}}$ as

$$C(\hat{\Delta}, \Phi) := \sum_{Y,i} \left\| \mathbf{v}_{Y,i}^+(\hat{\Delta}, \phi_{Y,i}^+) \right\|_2^2 + \left\| \mathbf{v}_{Y,i}^-(\hat{\Delta}, \phi_{Y,i}^-) \right\|_2^2. \quad (9)$$

The best-fitting cosines may not verify Eq. 1 and this must therefore be incorporated as a constraint in the fitting procedure. Denoting $\hat{h}_Y^\pm := \tilde{h}_Y^\pm - \hat{\Delta}$, the slopes of the cosines provide the first-order derivatives at their corresponding boundary points via

$$\frac{\partial}{\partial \theta} m_{Y,i}^\pm(\cdot, \theta_i) = -\hat{h}_{Y,i}^\pm \tan \phi_{Y,i}, \quad (10)$$

while the second-order derivatives can be obtained by finite differences of these first-order derivatives. To achieve this, the discrete second-order derivative operator \mathbf{D} is defined as

$$(\mathbf{D}\hat{h}_Y^\pm)_i := \frac{\frac{\partial}{\partial \theta} m_{Y,i+1}^\pm(\cdot, \theta_{i+1}) - \frac{\partial}{\partial \theta} m_{Y,i-1}^\pm(\cdot, \theta_{i-1})}{\theta_{i+1} - \theta_{i-1}}, \quad (11)$$

with boundary conditions for $k \in \{-1, N\}$, where N denotes the number of projections, given by

$$\begin{aligned} (\hat{h}_{Y,k}^\pm, \phi_{Y,k}^\pm) &= -(\hat{h}_{Y,k \bmod N}^\mp, \phi_{Y,k \bmod N}^\mp), \\ \theta_k &= \theta_{k \bmod N} + \pi \operatorname{sgn}(k). \end{aligned}$$

This allows the definition of the estimated discrete radii of curvature and express its constraint via

$$\hat{\rho}_X^\pm := (1 + \mathbf{D})\hat{h}_Y^\pm \quad (12a)$$

$$\text{s.t. } \pm \hat{\rho}_X^\pm \geq 0. \quad (12b)$$

The cosines are fitted around a set zero in the translational domain, thereby fixing the center of rotation at this position and determining shifts relative to it. As an initial guess, all relative phases are set to zero (thus satisfying Eq. 12b), and the shifts are initialized as the mean boundary positions, making the performance independent of the shifts. The minimization

of the cost function in Eq. 9 involves $N \times (1 + 2|\mathbb{Y}|)$ variables and therefore scales rapidly with the size of \mathbb{Y} . However, by approximating the min and max functions in Eq. 8 with smooth functions, highly sparse associated Jacobians and Hessians can be derived.

IV. RESULTS

The shift estimation results for phantoms A and B are shown in Fig. 6. Using the MAE to the GT shifts as metric, the algorithm performs best for phantom A, followed by phantom B. Most deviations from the GT are within one pixel; only 7 and 6 of the 360 projections exceed this for phantoms A and B, respectively, and none exceed two pixels. For phantom B, two outliers approach a two-pixel deviation. Reconstructions from the corrected sinograms, as shown in Fig. 7, show a substantial improvement over the uncorrected case and are close to the GT reconstructions. Attenuation artifacts are present in the reconstructions as this is not corrected for.

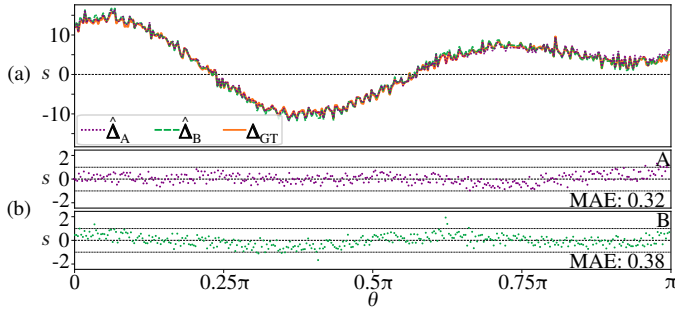


Fig. 6. Simulation results for shift estimations for phantoms A and B: (a) comparison between found and GT shifts, (b) residuals between found and GT shifts and their mean absolute error (MAE).

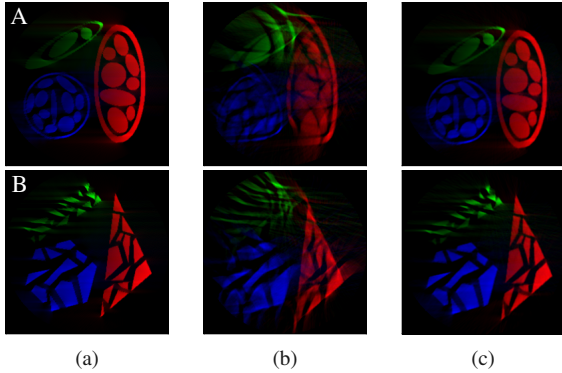


Fig. 7. Combined filtered backprojections of both phantoms: (a) using the GT geometry, (b) from the perturbed sinograms, and (c) from the sinograms corrected with the proposed method.

V. DISCUSSION

For both phantoms, shifts are estimated with near pixel-accuracy (Fig. 6), and correcting the sinograms accordingly yields substantially improved reconstruction qualities, nearing that of the GT.

In the ideal theoretical case, phantom B was expected to yield perfect performance. In practice, finite translational and

angular sampling limits the accuracy of the estimated radii of curvature, and the resulting discretization errors propagate into deviations from the ideal case. Since these radii provide the primary constraint on shift ambiguity, their imperfect estimation degrades calibration accuracy. Still, the outliers, specifically the point approaching a deviation of two pixels, are noteworthy. The empirically observed non-convexity of the optimization, with different initializations converging to distinct minima, plausibly explains these outliers and indicates the need for a more robust optimization approach.

Conversely, phantom A, despite its less constraining radii of curvature and larger set of admissible shifts, achieves the highest accuracy. This suggests that its admissible set is structured rather than uniform. The symmetry and smoothness of its supports may bias the optimization towards this solution, causing similar, but not equal, phantoms to converge to the same result. While this explains the strong performance, it also suggests that smooth samples may yield less reliable calibration performance.

In practice, boundary extraction will also be affected by noise and partial volume effects, but DCCs could also be formulated to assist in these issues. Finally, realistic datasets may contain substantially larger sets of sinograms than those considered here; such increased diversity may impose stronger cumulative constraints on the admissible shifts, further reducing ambiguity and potentially improving calibration accuracy.

VI. CONCLUSION

A novel tomographic calibration approach based on a pre-existing class of data consistency conditions is proposed and validated through numerical simulations. The method exploits sinogram support boundaries to recover shifts with respect to a chosen center of rotation. Provided these boundaries can be reliably extracted, the approach is invariant to attenuation effects, remains applicable to data acquired over half a rotation or less and does not require any reconstruction. Numerical simulations on shift-affected XFCT data demonstrate the effectiveness of the method. While applicable to a broader class of tomographic modalities, this work constitutes the first analytical calibration approach that is agnostic to attenuation effects in XFCT.

REFERENCES

- [1] S. Helgason, *The Radon Transform*, ser. Progress in Mathematics. Boston, MA, USA: Birkhäuser, 1999.
- [2] M. Guizar-Sicairos, A. Diaz, M. Holler, M. S. Lucas, A. Menzel, R. A. Wepf, and O. Bunk, “Phase tomography from x-ray coherent diffractive imaging projections,” *Opt. Express*, vol. 19, no. 22, pp. 21 345–21 357, 2011.
- [3] J. L. Prince and A. S. Willsky, “Estimation algorithms for reconstructing a convex set given noisy measurements of its support lines,” Massachusetts Institute of Technology, Laboratory for Information and Decision Systems, Cambridge, MA, Tech. Rep. LIDS-P-1638, 1987.
- [4] Z. Zhang, Z. Dong, H. Yan, A. Pattammattel, X. Bi, Y. Dong, G. Liu, X. Sun, and Y. Zhang, “A general image misalignment correction method for tomography experiments,” *iScience*, vol. 26, no. 10, p. 107932, 2023.
- [5] H. Ryan, “On extreme constant width bodies in \mathbb{R}^3 ,” *Discrete & Computational Geometry*, 2025.
- [6] N. R. Viganò and V. A. Solé, “Physically corrected forward operators for induced emission tomography: a simulation study,” *Measurement Science and Technology*, vol. 29, no. 3, p. 034005, 2018.